

Article

Spatial Distribution Analyses of Axially Long Plasmas under a Multi-Cusp Magnetic Field Using a Kinetic Particle Simulation Code KEIO-MARC

Ryota Nishimura¹, Tomohiro Seino¹, Keigo Yoshimura¹, Hiroyuki Takahashi¹, Akinobu Matsuyama², Kazuo Hoshino³ , Tetsutarou Oishi^{1,*}  and Kenji Tobita¹

¹ Department of Quantum Science and Energy Engineering, Tohoku University, Sendai 980-8579, Japan; nishimura.ryota.s5@dc.tohoku.ac.jp (R.N.); tomohiro.seino.p7@dc.tohoku.ac.jp (T.S.); keigo.yoshimura.s5@dc.tohoku.ac.jp (K.Y.); hiroyuki.takahashi.c6@tohoku.ac.jp (H.T.); kenji.tobita.d5@tohoku.ac.jp (K.T.)

² Graduate School of Energy Science, Kyoto University, Kyoto 611-0011, Japan; matsuyama.akinobu.3p@kyoto-u.ac.jp

³ Faculty of Science and Technology, Keio University, Yokohama 223-8522, Japan; hoshino@appi.keio.ac.jp

* Correspondence: tetsutarou.oishi.a4@tohoku.ac.jp

Abstract: To realize the development of a long plasma source with a uniform electron density distribution in the axial direction, the spatial distribution of plasma under a multi-cusp magnetic field was analyzed using a KEIO-MARC code. Considering a cylindrical plasma source with an axial length of 3000 mm and a cross-sectional diameter of 100 mm, in which the filament electrode was the electron source, the electron density distribution was calculated using the residual magnetic flux density, B_{res} , and the number of permanent magnets installed at different locations surrounding the device, N_{mag} , as design parameters. The results show that both B_{res} and N_{mag} improved the uniformity of the electron density distribution in the axial direction. The maximum axial electron density decreased with increasing N_{mag} and increased with increasing B_{res} . These trends can be explained by considering the nature of the multi-cusp field, where particles are mainly confined to the field-free region (FFR) near the center of the plasma column, and the loss of particles due to radial particle transport. The use of multiple filaments at intervals shorter than the plasma decay length dramatically improved axial uniformity. To further improve axial uniformity, the filament length and FFR must be properly set so that electrons are emitted inside the FFR.

Keywords: multi-cusp magnetic field; axially long plasma source; plasma spatial distribution; KEIO-MARC



Citation: Nishimura, R.; Seino, T.; Yoshimura, K.; Takahashi, H.; Matsuyama, A.; Hoshino, K.; Oishi, T.; Tobita, K. Spatial Distribution Analyses of Axially Long Plasmas under a Multi-Cusp Magnetic Field Using a Kinetic Particle Simulation Code KEIO-MARC. *Plasma* **2024**, *7*, 64–75. <https://doi.org/10.3390/plasma7010005>

Academic Editors: Tariq Rafiq and Andrey Starikovskiy

Received: 7 December 2023

Revised: 8 January 2024

Accepted: 18 January 2024

Published: 22 January 2024



Copyright: © 2024 by the authors. Licensee MDPI, Basel, Switzerland. This article is an open access article distributed under the terms and conditions of the Creative Commons Attribution (CC BY) license (<https://creativecommons.org/licenses/by/4.0/>).

1. Introduction

With regard to improving the plasma confinement performance of a plasma source, one of the primary methods involves applying a multi-cusp magnetic field to the plasma confinement region. A multi-cusp magnetic field is generated through the placement of multiple permanent magnets around the vessel wall in a circumferential configuration. Assuming a cylindrical vessel is being used, a magnetic field with components exclusively within a plane perpendicular to the cylinder axis is generated. This magnetic field configuration is widely used in plasma sources because of its role in confining the plasma and reducing particle loss. The applications of multi-cusp magnetic fields encompass a broad spectrum of topics [1–12]. The most common application resides in the field of ion source development, where these fields have yielded enhancements in the confinement of hot and bulk electrons [13,14]. In the context of nuclear fusion research, investigations into plasma–wall interactions have been conducted by employing an AIT-PID (Aichi Institute of Technology Plasma Irradiation Device, Aichi, Japan) equipped with a multi-cusp magnetic

field plasma source [15–18]. Furthermore, one potential method for studying atomic processes is an experiment in which ion/electron beams are injected into plasma confined by a multi-cusp magnetic field. The attenuation of the injected beam depends on $n_t\sigma L$, where n_t , σ , and L denote the density of the target plasma particles, the reaction cross-section, and plasma length, respectively. Consequently, an extended plasma length in the axial direction becomes essential to facilitate the precise observation of beam attenuation caused by collisions between the plasma and the beam. Given that the number of plasma–beam collisions per unit volume and unit time is expressed as $n_t n_b \langle \sigma v \rangle$, using the beam density n_b and the beam velocity v , the importance of the spatial distribution of the target plasma density must also be noted. Specifically, high-density target plasma with a uniform density distribution enables the clear observation of the impact of the injected beam on the target plasma. To control the spatial distribution of plasma density, it is critical to understand the mechanism of particle loss. Under conditions of relatively high electron temperatures and negligible volume recombination, the axial distribution of electron density is significantly dependent on radial losses. In systems with axial magnetic fields, collisions during Larmor motion produce radial losses. Conversely, the axial field strength within the multi-cusp magnetic field is practically zero, which differs in the radial loss mechanism from plasma experiments characterized by an axial magnetic field [19,20]. Particularly noteworthy is the mechanism that determines the spatial distribution of the plasma within a multi-cusp magnetic field in an axially long plasma source, which has not yet been understood. Therefore, the purpose of this paper is to analyze the spatial distribution of axially extended plasma in a multi-cusp magnetic field via numerical simulation and to suggest a methodology necessary for achieving a uniform plasma distribution.

2. Simulation Model

2.1. Plasma Source

A schematic diagram of the plasma source is depicted in Figure 1. The plasma source was configured with the following dimensions: a diameter of 100 mm and a length of 3000 mm. Throughout the calculations, the potential of the plasma source, including both ends, was consistently maintained at a floating potential, which was determined by the electron temperature near the wall. Permanent magnets were placed on the sidewall of the plasma source parallel to the cylindrical axis. Magnets were not placed at either end of the plasma source. In the actual fabrication of the device, it is expected that multiple magnets of realistic sizes would be placed on the wall surface in a straight line parallel to the cylindrical axis. This would leave a small gap between the aligned magnets, but this gap was neglected in the numerical calculations in this study.

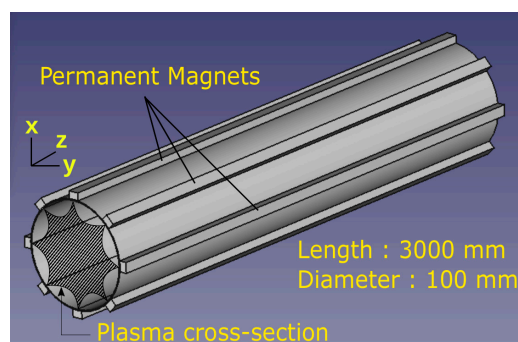


Figure 1. Schematic of plasma source with multi-cusp magnetic field.

2.2. Calculation of Multi-Cusp Magnetic Field

The utilization of multi-cusp magnetic fields is one of the methods employed to improve the confinement of plasma. Furthermore, it serves to establish a uniform radial distribution of the bulk plasma. While there are many techniques for the generation of a multi-cusp magnetic field, the configuration based on a line–cusp arrangement represents

an optimized approach for plasma confinement [21]. Therefore, the line-cusp arrangement was employed in this study. The magnetic field at each spatial point was calculated using the principles of magnetic Coulomb's law, as expressed by the following equation:

$$d\mathbf{H} = \frac{B_{res}dS}{4\pi\mu_0r^2}\hat{r} \quad (1)$$

where B_{res} , μ_0 , and \hat{r} denote the residual magnetic flux density, vacuum permeability, and unit position vector originating from the area element of the magnet surface, respectively. The dimensions of the magnet, as well as the separation between the poles, were set to 10 mm and 20 mm, respectively. The magnet surface was divided into a 0.5 mm \times 0.5 mm grid, thus rendering dS equal to 2.5×10^{-7} m². In practice, a supporting plate would be interposed between the magnets and the plasma. In this study, the thickness of this support plate was set to 1 mm. Consequently, the magnets were positioned at a distance of 1 mm away from the wall. Note that Equation (1) implies a divergence of the magnetic field strength close to the surface of the magnet, which can be avoided by placing the magnet slightly outside of the wall. The number of permanent magnets installed around the device, N_{mag} , is also an important parameter that determines the characteristics of a multi-cusp magnetic field. N_{mag} must be an even number for the line-cusp configuration. Calculations were performed for all the magnets of the device. Furthermore, since both B_{res} and N_{mag} affect the spatial distribution of the plasma, B_{res} and N_{mag} were given separately as independent parameters in the calculations.

2.3. Calculation of Electron Energy Distribution Function

The Electron Energy Distribution Function (EEDF) in space was analyzed using a KEIO-MARC (kinetic model of electrons in ion source with multi-cusp ARC discharge) code [22–26]. KEIO-MARC has been used to estimate the H^- production rate in a negative ion source called an SHI H^- ion source [27,28] and improve the performance of a JT-60SA negative ion source [29] and for comparison with the results of spectroscopic measurements taken from a QST (National Institute of Quantum and Radiological Science and Technology, Naka, Japan) 10-ampere ion source [30].

Input parameters were provided to the KEIO-MARC code pertaining to the chamber geometry, filament configuration, and multi-cusp magnetic field. In addition, the density of each background particle (H , H_2 , H^+ , H_2^+ , and H_3^+) was determined prior to the calculations. Although the KEIO-MARC code possesses the ability to accommodate over 500 elastic/inelastic and Coulomb collisions in the context of hydrogen plasmas, this study simplifies the corresponding analysis by considering only 38 reactions involving the five aforementioned particles. The fundamental equation governing KEIO-MARC is expressed as follows [22]:

$$m_e \frac{d\mathbf{v}_e}{dt} = -e(\mathbf{E} + \mathbf{v}_e \times \mathbf{B}) + m_e \left(\frac{\delta\mathbf{v}_e}{\delta t} \right)_{collision}, \quad (2)$$

where m_e , \mathbf{v}_e , e , \mathbf{E} , and \mathbf{B} are the electron mass, velocity, charge, electric field, and multi-cusp magnetic field, respectively. Quasi-neutrality was assumed since the Debye length in the plasma region ($T_e \sim 6$ eV, $n_e \sim 10^{15}$ m⁻³) is less than 1 mm, which is much shorter than the system length. Under the assumption of quasi-neutrality, except at the plasma source surface and filament, the electric field E is exclusively considered within the boundary regions corresponding to the wall and filament. Sheath boundary conditions are applied to both ends and the sidewall, featuring a potential (ϕ_{sh}) described by

$$\phi_{sh} = \frac{k_B T_e}{2e} \ln \frac{m_i}{2\pi m_e}, \quad (3)$$

where k_B , T_e and m_i represent the Boltzmann constant, electron temperature, and ion mass, respectively. At both ends and at the sidewall, electrons characterized by energies lower than $e\phi_{sh}$ are reflected by the sheath, while those with energies higher than $e\phi_{sh}$ are

lost. The update time intervals for the electron orbit calculations, Coulomb collisions, and elastic/inelastic collisions were set to 10^{-11} , 10^{-9} , and 10^{-8} s, respectively.

In the simulations reported in this study, it is assumed that the plasma has been generated through the implementation of a DC arc discharge featuring hot cathodes. While it is a common practice to position the filament at the periphery of the plasma source, this study adopts a distinct approach, inserting the filament within the central region of the plasma source with the aim of achieving a uniform plasma distribution. For the investigation of reference plasma distributions reported in Sections 3.1 and 3.2, a solitary filament was employed. In the investigation reported in Section 3.3, multiple filaments were employed in pursuit of uniform plasma. In this context, a hairpin-shaped filament was employed. The filament exhibited a composite structure, comprising a linear segment and a semicircular section with respective lengths and radii of 35 mm and 10 mm (resulting in a total length of 45 mm). The filament emits electrons from its surface, and the bulk neutrals in the plasma source are ionized. The energy and emission counts were determined by the arc voltage and current, set to 100 V and 10 A in this study. It is worth noting that the thickness of the sheath region is sufficiently shorter than the respective dimensions of the plasma source so that electrons are instantly accelerated by the arc voltage. Since quasi-neutrality was assumed in the plasma region, our use of arc voltage for the initial velocity of the electrons is justified. The initial positions of the emitted electrons were randomly determined, and the electrons were emitted perpendicular to the filament surface; the total scattering cross section of the hydrogen molecule for a 100 eV electron is 2.54×10^{-20} m² [31]. The higher the hydrogen molecular pressure, the greater the decrease in the electron density in the axial direction. Subsequently, electron energy is lost mainly through collisions. In this study, the hydrogen molecular pressure was set to 0.2 Pa. Under a hydrogen molecular pressure of 0.2 Pa and a temperature of 500 K, the electron mean free path λ was estimated to be 1.36 m. Since λ is shorter than the system length of 3 m, the decay in electron density in the axial direction is significant. The temperatures and densities of the background particles are comprehensively documented in Table 1.

Table 1. Temperature and density of the background particles.

Particle	Temperature (K)	Density (m ⁻³)
H ₂	500	2.9×10^{19}
H	1000	2.9×10^{17}
H ⁺	5800	1.0×10^{17}
H ₂ ⁺	1000	1.0×10^{15}
H ₃ ⁺	1000	1.0×10^{15}

The KEIO-MARC code calculates the trajectories of electrons emitted from the filament and secondary electrons produced through ionization, considering the magnetic field and collisions between particles. The calculations continue until EEDF, $f_e(E)$, reaches a steady state. The EEDF at each point in space is evaluated based on the position and velocity of each electron. The electron density, n_e , and the averaged energy, $\langle E \rangle$, are calculated as follows:

$$n_e = \int_0^{E_{max}} f_e(E) dE, \quad (4)$$

$$\langle E \rangle = \frac{1}{n_e} \int_0^{E_{max}} f_e(E) E dE, \quad (5)$$

where E_{max} is the calculated maximum energy (150 eV in this paper) and $\langle E \rangle$ is evaluated as the averaged energy of hot electrons emitted from the filament and the bulk plasma. The electron temperature T_e was calculated from the gradient of the Electron Energy Probability Function (EEDF) defined by $f_e(E)/\sqrt{E}$ in the low-temperature region (<10 eV). The typical results calculated using KEIO-MARC for the axial distribution of the EEDF and the EEDF at $z = 1000$ mm are shown in Figures 2a and 2b, respectively.

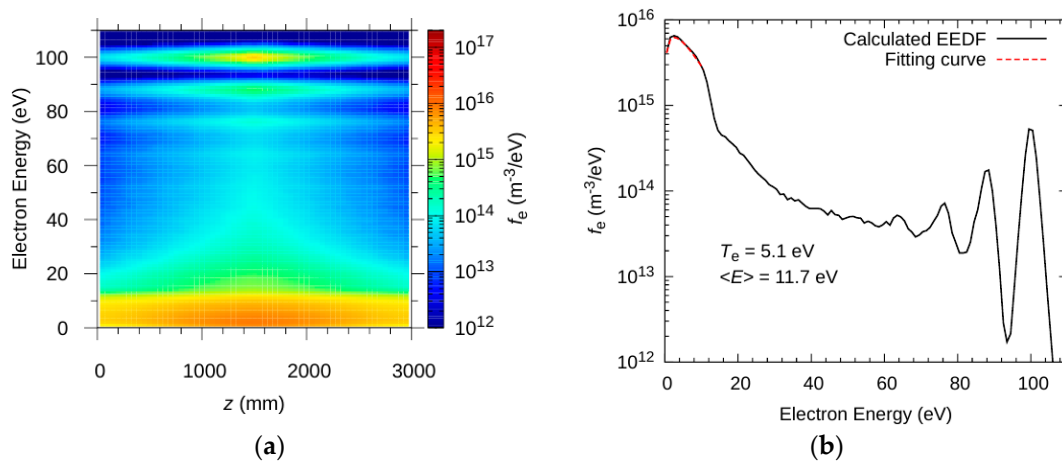


Figure 2. Typical calculated EEDF (a) axial distribution on the centerline ($x = y = 0$ mm) and (b) $z = 1000$ mm. The dashed red curve shows the Maxwell distribution fit to the EEPF in the region below 10 eV.

As described above, the filament was inserted at $z = 1500$ mm, with an arc voltage of 100 V. Therefore, the EEDF exhibited a peak of approximately 100 eV at $z = 1500$ mm, as shown in Figure 2a,b. The electrons were initially accelerated by the sheath potential formed around the filament and then lost their energy through collisions with the bulk particles. The amount of energy lost in collisions is unique to each of the various types of elementary processes that occur in collisions. Therefore, several energy peaks appeared in the EEDF in the relatively high-energy region. As shown in Figure 2a, high-energy electrons were found even at both ends of the plasma source, indicating that some electrons reached both ends without experiencing a significant loss of energy. As shown in Figure 2b, the EEDF became continuous in the relatively low-energy region; thus, T_e was calculated from the gradient of the EEDF.

3. Simulation Results

A typical multi-cusp magnetic field distribution is shown in Figure 3. Here, B_{res} and N_{mag} are set to 0.75 T and 8, respectively.

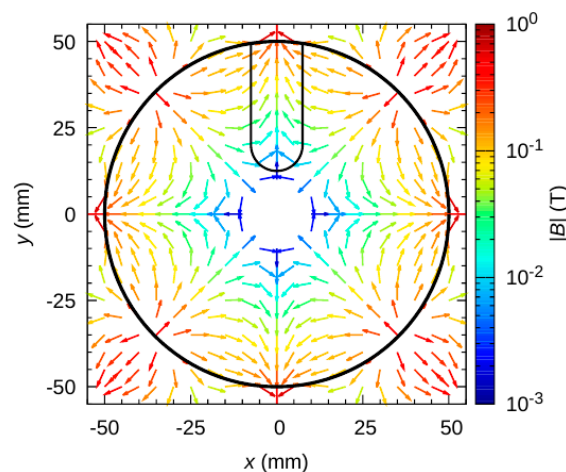


Figure 3. Typical multi-cusp magnetic field distribution of the cross-section. The B_{res} and N_{mag} are 0.75 T and 8, respectively. The solid black curve indicates a filament.

In the multi-cusp magnetic field, the strength of the magnetic field increases from the center to the wall and is greatest near the wall. The charged particles in the plasma are reflected at the wall's surface owing to the magnetic field gradient. Note that B_z is almost

zero except near the edge of the plasma source. A region with a weak magnetic field is distributed around the center; it is called the field-free region (FFR). The FFR is one of the significant parameters that characterizes a multi-cusp magnetic field because the plasma is mainly distributed inside of it. In this study, the FFR was defined as the diameter of the circular cross section where the magnetic field strength is less than 5 mT in the line-cusp magnetic configuration. The typical electron density distribution of the cross section is shown in Figure 4.

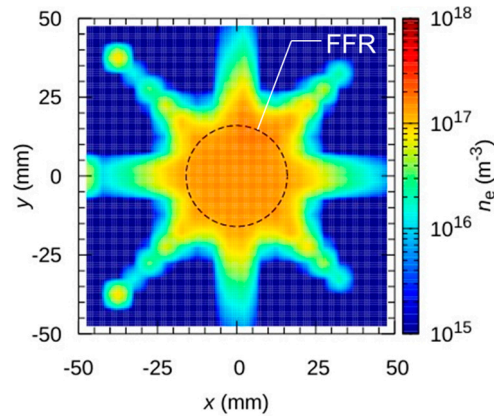


Figure 4. Typical electron density distribution of the cross-section. The B_{res} and N_{mag} are 0.75 T and 8, respectively. The region within the dashed circle represents a field-free region.

Electrons were mainly distributed in the FFR, as represented by the black dashed circle in Figure 4. However, electrons were lost on the surface of the magnets, forming a line-cusp configuration. The plasma was uniformly distributed within the FFR. Thus, the multi-cusp magnetic field played a key role in generating uniform plasma in the radial direction.

3.1. Effect of the Radial Magnetic Flux Density B_{res} on Plasma Axial Distribution

B_{res} is effective in improving plasma confinement. Analyses were performed in which the value of B_{res} was varied from 0.25 T to 1 T. In this section, N_{mag} and the position of the filament z_{fil} were fixed at 10 and 1500 mm, respectively. The distributions of n_e , T_e , and $\langle E \rangle$ on the centerline ($x = y = 0$ mm) in the axial direction are shown in Figure 5.

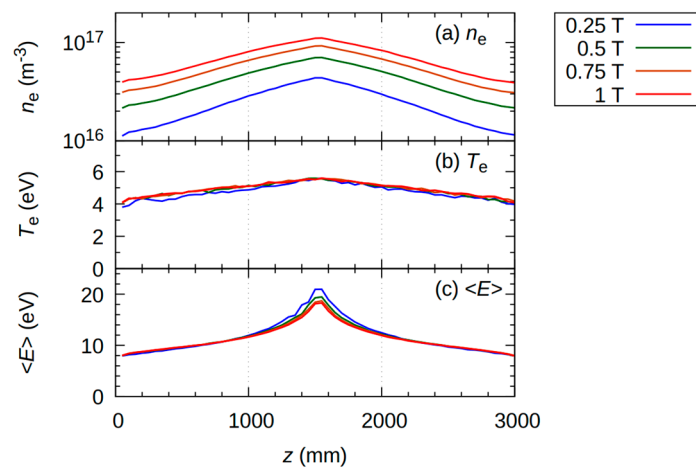


Figure 5. Axial distribution of (a) n_e , (b) T_e , and (c) $\langle E \rangle$ on the centerline ($x = y = 0$ mm) as a function of the residual magnetic flux density B_{res} . The position of the inserted filament and number of magnets were $z = 1500$ mm and 10, respectively.

The electron density peaked at the filament position ($z = 1500$ mm) and decreased as the distance from the filament increased (Figure 5a). However, it increased over the entire volume of the plasma source as the B_{res} increased. On the other hand, electron temperature was independent of B_{res} , with a maximum value of approximately 5.5 eV at the filament position, and decreased by approximately 1 eV at both ends of the plasma source. The average electron energy $\langle E \rangle$ tends to be similar to T_e , with a weak dependence on B_{res} . The electron density distribution is considered to depend on the FFR and losses at the boundary wall. Note that the electron losses due to volume recombination can be neglected in the calculations being discussed. The size of the FFR depends on B_{res} , as shown in Figure 6a.

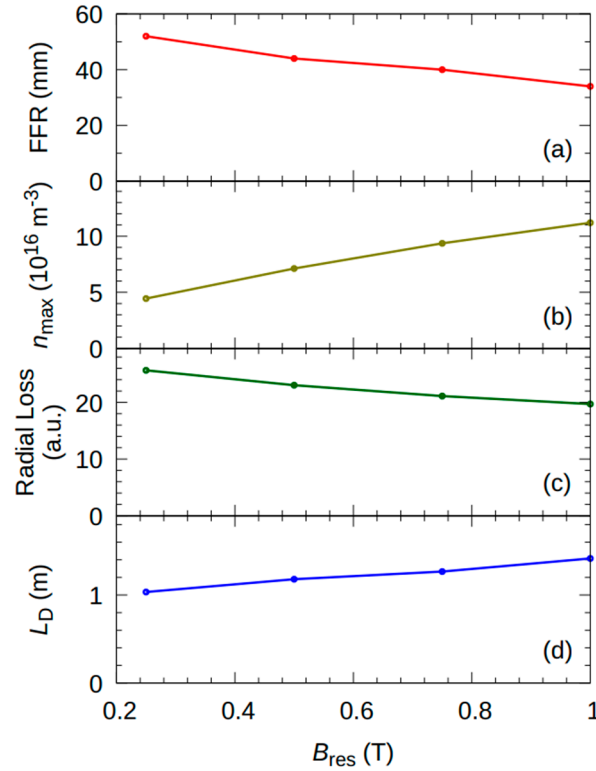


Figure 6. Dependence of (a) FFR, (b) maximum electron density n_{max} , (c) radial electron loss, and (d) decay length L_D on B_{res} . FFR is defined as the diameter of the circular cross-section, where the magnetic field strength is less than 5 mT.

The dependence of the maximum electron density (n_{max}) is summarized in Figure 6b. The radial losses plotted in Figure 6c were calculated based on the total number of electrons that reached the sidewall of the plasma source. The uniformity of electron density was of interest in this study. The distribution of n_e appears to be linear on the logarithmic axis. Therefore, the distribution of n_e was assumed to decrease exponentially when moving away from the filament. To quantitatively evaluate the plasma decay length (L_D), the axial distribution of n_e was fitted with an exponential function, as follows:

$$n_e(z) = n_{max} \exp\left(-\frac{|z - z_{fil}|}{L_D}\right). \quad (6)$$

The FFR decreased with an increase in B_{res} . This is considered to narrow the region over which the plasma is distributed and increase n_{max} . In addition, the radial electron losses were reduced. This effect also contributes to an increase in n_e , resulting in improved L_D . Therefore, an increase in B_{res} is important for obtaining uniform electron density in the

axial direction. However, the effect of B_{res} on preventing the axial decay of $\langle E \rangle$ is negligible, and other approaches are required.

3.2. Effect of the Number of Magnets N_{mag} on Plasma Axial Distribution

Next, we discuss the effect of the number of magnets N_{mag} on the plasma axial distribution. An analysis was performed using a N_{mag} of 6–12 and a B_{res} of 0.75 T. The axial distributions of n_e , T_e , and $\langle E \rangle$ as functions of N_{mag} are shown in Figure 7.

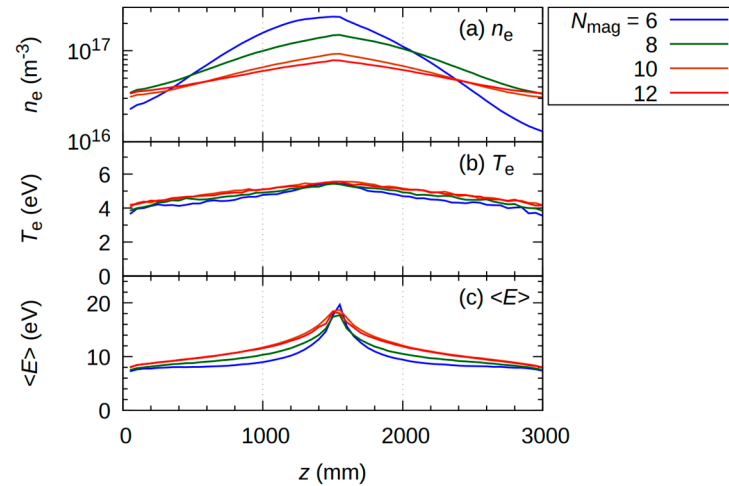


Figure 7. Axial distributions of (a) n_e , (b) T_e , and (c) $\langle E \rangle$ on the centerline ($x = y = 0$ mm) as functions of N_{mag} . The position of the inserted filament and the residual magnetic flux density are $z_{fil} = 1500$ mm and 0.75 T, respectively.

The electron density n_e decreased when moving away from the filament, as shown in Figure 5. The maximum value of n_e decreased with increasing N_{mag} . The electron temperature T_e followed the same tendency as that shown in Figure 5. On the other hand, the $\langle E \rangle$ distributions have roughly the same peak value near the filament, but the axial decay is mitigated by the increasing N_{mag} . Similar to Figure 5, this tendency can also be interpreted using the FFR and radial transport losses. Figure 8 shows the dependence of the (a) FFR, (b) n_{max} , (c) radial electron losses, and (d) L_D on N_{mag} . Here, the distributions of n_e were again assumed to decrease exponentially when moving away from the filament, except in the case of $N_{mag} = 6$.

Increasing N_{mag} weakened the radial component of the multi-cusp magnetic field and expanded the FFR. This also expanded the area over which the plasma was distributed, resulting in a decrease in n_{max} . In addition, as the size of the FFR increased, the radial gradient of the multi-cusp magnetic field increased, and thus the lifetime of the electrons extended, resulting in the mitigation of the decay of $\langle E \rangle$. The radial electron losses decreased slightly with increasing N_{mag} . An increase in N_{mag} decreased the distance between adjacent magnets and increased the maximum magnetic field strength near the chamber wall [5]. The slight decrease in radial loss was due to this effect. The L_D increased with increasing N_{mag} . Although it is difficult to reduce electron losses significantly by increasing N_{mag} , this action extends the electron lifetime and improves axial uniformity. Therefore, N_{mag} is another important factor for obtaining axially uniform plasma.

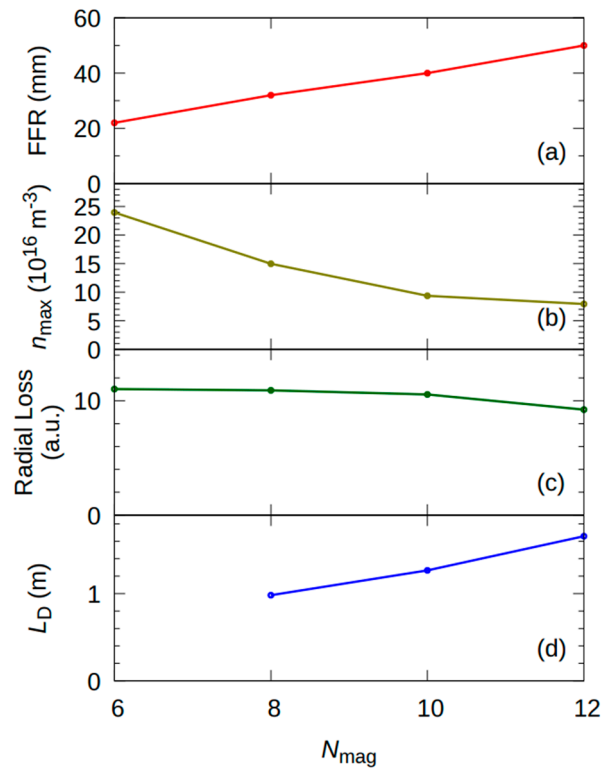


Figure 8. Dependence of (a) FFR, (b) n_{max} , (c) radial electron losses, and (d) L_D on N_{mag} . FFR is defined as the diameter of the circular cross section where the magnetic field strength is less than 5 mT.

For $N_{\text{mag}} = 6$ in Figure 7, an asymmetric electron density distribution was obtained at around $z_{\text{fil}} (=1500 \text{ mm})$. In this case, the size of the FFR was approximately 20 mm, and the outer half of the filament was located outside the FFR, which has a strong radial magnetic field. Thus, some of the emitted electrons were immediately trapped in the multi-cusp magnetic field. This generated a magnetic field gradient (grad- B) drift, and electrons were transported in one direction. Figure 9a,b show the electron density distributions on the YZ cross section for $N_{\text{mag}} = 6$ and 12, respectively.

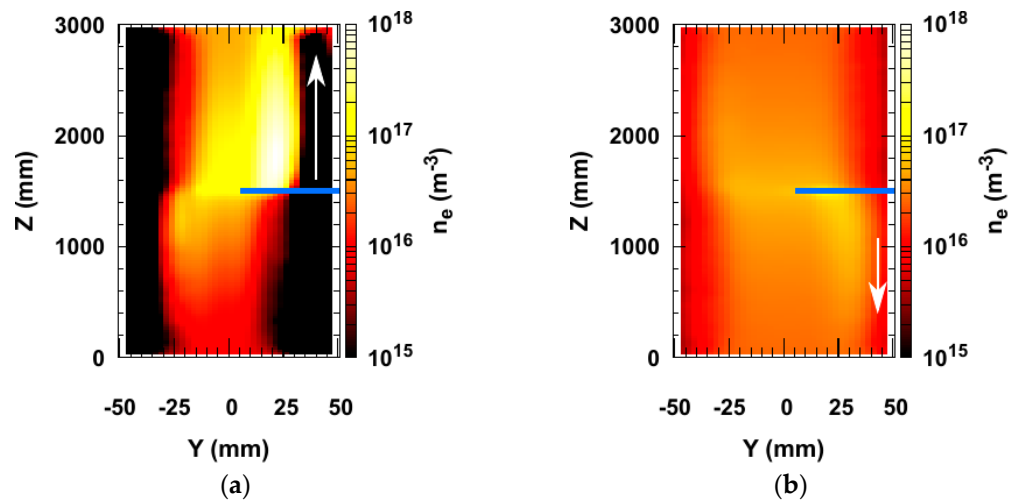


Figure 9. Cross-section of n_e distribution (a) $N_{\text{mag}} = 6$ and (b) $N_{\text{mag}} = 12$ on the YZ plane ($x = 0 \text{ mm}$). The filament was inserted at $z_{\text{fil}} = 1500 \text{ mm}$ and drawn as a blue solid line.

For $N_{\text{mag}} = 6$, the electrons emitted from the filament were transported in one direction toward $z = 3000$ mm. At the location of the filament, the magnetic field and magnetic field gradient vectors were in the negative direction along the X-axis and along the Y-axis, respectively. Then, electrons were transported along the Z-axis via grad-B drift. Consequently, the electron density distribution was asymmetrical in the axial direction. This is a serious impediment to axially uniform plasma generation. In contrast, the FFR increased from 20 to 55 mm as N_{mag} increased from 6 to 12. Thus, electrons were emitted inside the FFR, and the asymmetry was mitigated. Therefore, in axially long plasmas, it is necessary to place the filaments deeper or to adjust the FFR by B_{res} and N_{mag} to emit electrons inside the FFR.

3.3. Effect of Increasing the Number of Filaments on the Axial Plasma Distribution

Finally, we will discuss the number of filaments (N_{fil}). In the previous subsections, only one filament was inserted at $z = 1500$ mm. However, it is difficult to generate a uniform plasma with a single filament in a 3 m plasma source. Therefore, multiple filaments were used. The axial distribution of the plasma was analyzed by placing up to six filaments at equal intervals. The axial distributions of n_e , T_e , and $\langle E \rangle$ as functions of N_{fil} are shown in Figure 10.

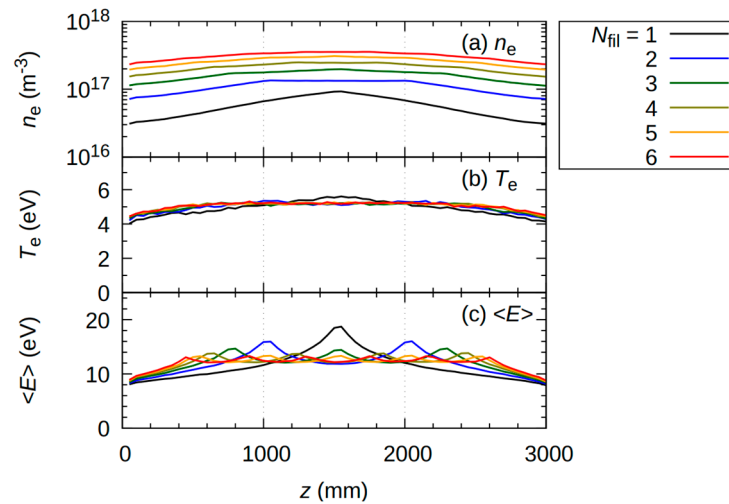


Figure 10. Axial distributions of (a) n_e , (b) T_e , and (c) $\langle E \rangle$ on the centerline ($x = y = 0$ mm) as a function of the number of filaments N_{fil} . The residual magnetic flux density and the number of magnets are 0.75 T and 8, respectively.

The insertion of multiple filaments increases the maximum electron density and mitigates axial non-uniformity. Here, the coefficients of variation (defined by the standard deviation per average value) of the axial electron density distribution were improved from 0.34 to 0.21, 0.17, 0.15, 0.13, and 0.13 upon increasing N_{fil} from 1 to 2, 3, 4, 5, and 6 (the corresponding filament intervals were 100, 75, 60, 50, and 43 cm), respectively. Furthermore, the axial non-uniformity was improved for $\langle E \rangle$ distribution. The decay length L_D , defined in Equation (6), is the distance over which n_{max} decreases by a factor of $1/e \approx 37\%$. Indeed, by placing the filaments at intervals approximately equal to L_D (=98 cm in this case), the uniformity of the electron density distribution was only within 37%. By placing filaments at appropriate intervals, the hot primary electrons that ionize the neutral particles are freely distributed throughout the plasma source, resulting in uniform plasma. If an even more stringent requirement is imposed on the uniformity of the axial electron density distribution, the filaments should be placed at intervals even shorter than those of the L_D .

4. Conclusions

The spatial distribution of axially long plasmas in a multi-cusp magnetic field was analyzed using a KEIO-MARC code. Considering a cylindrical plasma source with an axial length of 3000 mm and a cross-sectional diameter of 100 mm, in which the filament electrode is the electron source, the electron density distribution was calculated using B_{res} and N_{mag} as design parameters. The results showed that both B_{res} and N_{mag} improve the uniformity of the electron density distribution in the axial direction. B_{res} was important for reducing radial electron losses. As a result, n_e increased at each axial point, and non-uniformity was mitigated. N_{mag} also plays a key role in mitigating the axial non-uniformities of n_e and $\langle E \rangle$ distributions. However, increasing N_{mag} caused the plasma to be distributed over a wider area, and the maximum value of n_{max} decreased. Both B_{res} and N_{mag} increase the decay length and mitigate axial non-uniformity, but with a tradeoff consisting of higher electron density.

We considered a plasma source with a diameter of 10 cm, indicating that the area size of the FFR in the plasma confinement region needs to be taken into account. If the FFR is narrow and the electrons emitted from the filament are trapped by the multi-cusp magnetic field, the axial distribution of the electron density would be asymmetric owing to grad- B drift. To avoid an axially asymmetric density distribution, the FFR should be adjusted by one of or both B_{res} and N_{mag} , or the filament should be inserted deeper. Furthermore, the decay length L_D was also shown to be an important parameter in the generation of a long and uniform plasma in the axial direction. In order to achieve a uniform axial distribution of n_e , T_e , and $\langle E \rangle$, the filaments needed to be placed at intervals shorter than L_D . For a hydrogen molecular pressure of 0.2 Pa, L_D was shorter than the mean free path of the electrons. L_D depends not only on the molecular hydrogen pressure but also on the multi-cusp field conditions, B_{res} , and N_{mag} , as previously mentioned, and these factors should also be taken into account when determining the filament arrangement.

Author Contributions: Conceptualization, R.N., T.O., and K.T.; methodology, R.N., H.T., A.M., T.O., and K.T.; software, R.N. and K.H.; validation, R.N., H.T., T.O., and K.T.; formal analysis, R.N.; investigation, R.N., T.S., K.Y., H.T., T.O., and K.T.; resources, H.T., T.O., and K.T.; data curation, R.N., T.S., K.Y., H.T., T.O., and K.T.; writing—original draft preparation, R.N.; writing—review and editing, H.T., A.M., and T.O.; visualization, R.N.; supervision, T.O.; project administration, K.T.; funding acquisition, H.T. All authors have read and agreed to the published version of the manuscript.

Funding: This work was partially supported by JSPS KAKENHI under grant number JP20H01883.

Institutional Review Board Statement: Not applicable.

Informed Consent Statement: Not applicable.

Data Availability Statement: Data are available on request.

Conflicts of Interest: The authors declare no conflicts of interest.

References

1. Takeiri, Y.; Ando, A.; Keneko, O.; Oka, Y.; Akiyama, R.; Asano, R.; Kawamoto, T.; Kuroda, T.; Tanaka, M.; Kawakami, H. Development of an intense negative hydrogen ion source with an external magnetic filter. *Rev. Sci. Instrum.* **1995**, *66*, 2541–2546. [[CrossRef](#)]
2. Takeiri, Y. Negative ion source development for fusion application. *Rev. Sci. Instrum.* **2010**, *81*, 02B114. [[CrossRef](#)]
3. Jayamanna, K.; Ames, F.; Bylinskii, I.; Lovera, M.; Minato, B. A 60 mA DC H⁻ multi cusp ion source developed at TRIUMF. *Nucl. Instrum. Methods Phys. Res. A* **2018**, *895*, 150–157. [[CrossRef](#)]
4. Jia, X.; Zhang, T.; Zheng, X.; Qin, J. Development of a compact filament-discharge multi-cusp H⁻ ion source. *Rev. Sci. Instrum.* **2013**, *83*, 02A730. [[CrossRef](#)]
5. Kim, J.H. Numerical simulation of a multi-cusp ion source for high current H⁻ cyclotron at RISP. *Phys. Procedia* **2015**, *66*, 498–505. [[CrossRef](#)]
6. Ohara, Y.; Akiba, M.; Horiike, H.; Inami, H.; Okumura, Y.; Tanaka, S. 3D computer simulation of the primary electron orbits in a magnetic multipole plasma source. *J. Appl. Phys.* **1987**, *61*, 1323–1328. [[CrossRef](#)]
7. Hoseinzade, M.; Nijatie, A. Development of H⁻ multicusp ion source. *Radiat. Detect. Technol. Meth.* **2018**, *2*, 27. [[CrossRef](#)]
8. Wicker, T.E.; Mantei, T.D. Plasma etching in a multipolar discharge. *J. Appl. Phys.* **1985**, *57*, 1638. [[CrossRef](#)]

9. Cooper, C.M.; Weisberg, D.B.; Khalzov, I.; Milhone, J.; Flanagan, K.; Peterson, E.; Wahl, C.; Forest, C.B. Direct measurement of the plasma loss width in an optimized, high ionization fraction, magnetic multi-dipole ring cusp. *Phys. Plasmas* **2016**, *23*, 102505. [[CrossRef](#)]
10. Jiang, Y.; Fubiani, G.; Garrigues, L.; Boeuf, J.P. Magnetic cusp confinement in low- β plasmas revisited. *Phys. Plasmas* **2020**, *27*, 113506. [[CrossRef](#)]
11. Patel, A.D.; Sharma, M.; Ramasubramanian, N.; Ganesh, R.; Chattopadhyay, P.K. A new multi-line cusp magnetic field plasma device (MPD) with variable magnetic field. *Rev. Sci. Instrum.* **2018**, *89*, 043510. [[CrossRef](#)]
12. Patel, A.D.; Sharma, M.; Ramasubramanian, N.; Ghosh, J.; Chattopadhyay, P.K. Characterization of argon plasma in a variable multi-pole line cusp magnetic field configuration. *Phys. Scr.* **2020**, *95*, 035602. [[CrossRef](#)]
13. Leung, K.N.; Samec, T.K.; Lamn, A. Optimization of permanent magnet plasma confinement. *Phys. Lett.* **1975**, *51*, 490–492. [[CrossRef](#)]
14. Leung, K.N.; Taylor, G.R.; Barrick, J.M.; Paul, S.L.; Kribel, R.E. Plasma Confinement by permanent magnet boundaries. *Phys. Lett.* **1976**, *57*, 145–147. [[CrossRef](#)]
15. Takamura, S. Characteristics of the compact plasma device AIT-PID with multicusp magnetic confinement. *IEEJ Trans.* **2012**, *7* (Suppl. S1), S19–S24. [[CrossRef](#)]
16. Takamura, S.; Ohno, N.; Nishijima, D.; Kajita, S. Formation of Nanostructured Tungsten with Arborescent Shape due to Helium Plasma Irradiation. *Plasma Fus. Res.* **2006**, *1*, 051. [[CrossRef](#)]
17. Takamura, S.; Tsujikawa, T.; Tomida, T.; Suzuki, K.; Minagawa, T.; Miyamoto, T.; Ohno, N. Compact Plasma Device for PWI Studies. *J. Plasma Fusion Res. Ser.* **2010**, *9*, 441–445.
18. Takamura, S.; Uesugi, Y. Coupled interactions between tungsten surfaces and transient high-heat-flux deuterium plasmas. *Nucl. Fusion* **2015**, *55*, 033003. [[CrossRef](#)]
19. Nishijima, D.; Ye, M.Y.; Ohno, N.; Takamura, S. Formation mechanism of bubbles and holes in tungsten surface with low-energy and high-flux helium plasma irradiation in NAGDIS-II. *J. Nucl. Mater.* **2004**, *329–333*, 1029–1033. [[CrossRef](#)]
20. Okamoto, A.; Kado, S.; Kajita, S.; Tanaka, S. Laser Thomson scattering system applicable to low-temperature plasma in the divertor simulator MAP-II. *Rev. Sci. Instrum.* **2005**, *76*, 116106. [[CrossRef](#)]
21. Hosseinzadeh, M.; Afarideh, H. Numerical simulation for optimization of multipole permanent magnets of multicusp ion source. *Nucl. Instrum. Methods Phys. Res. A* **2014**, *735*, 416–421. [[CrossRef](#)]
22. Hatayama, A.; Nishioka, S.; Nishida, K.; Mattei, S.; Lettry, J.; Miyamoto, K.; Shibata, T.; Onai, M.; Abe, S.; Fujita, S.; et al. Present status of numerical modeling of hydrogen negative ion source plasmas and its comparison with experiments: Japanese activities and their collaboration with experimental groups. *New J. Phys.* **2018**, *20*, 065001. [[CrossRef](#)]
23. Shibata, T.; Kashiwagi, M.; Inoue, T.; Hatayama, A.; Hanada, M. Numerical study of atomic production rate in hydrogen ion sources with the effect of non-equilibrium electron energy distribution function. *J. Appl. Phys.* **2013**, *114*, 143301. [[CrossRef](#)]
24. Hatayama, A.; Shibata, T.; Nishioka, S.; Ohta, M.; Yasumoto, M.; Nishira, K.; Yamamoto, T.; Miyamoto, K.; Fukano, A.; Mizuno, T. Kinetic modeling of particle dynamics in H^- negative ion sources. *Rev. Sci. Instrum.* **2014**, *85*, 02A510. [[CrossRef](#)]
25. Kato, R.; Hoshino, K.; Nakano, H.; Shibata, T.; Miyamoto, K.; Iwanaka, K.; Hayashi, K.; Hatayama, A. Numerical analysis of isotope effect in NIFS negative ion source. *J. Phys. Conf. Ser.* **2022**, *2244*, 012035. [[CrossRef](#)]
26. Onai, M.; Etoh, H.; Aoki, Y.; Shibata, T.; Mattei, S.; Fujita, S.; Hatayama, A.; Lettry, J. Effect of high energy electrons on H^- production and destruction in a high current DC negative ion source for cyclotron. *Rev. Sci. Instrum.* **2016**, *87*, 02B127. [[CrossRef](#)] [[PubMed](#)]
27. Etoh, H.; Onai, M.; Aoki, Y.; Mitsubori, H.; Arakawa, Y.; Sakuraba, J.; Kato, T.; Mitsumoto, T.; Hiasa, T.; Yajima, S.; et al. High current DC negative ion source for cyclotron. *Rev. Sci. Instrum.* **2016**, *87*, 02B135. [[CrossRef](#)]
28. Yamada, S.; Kitami, H.; Nomura, S.; Aoki, Y.; Hoshino, K.; Hatayama, A. Numerical Simulation for Enhancement of H^- Production in the DC Arc-Discharge Hydrogen Negative Ion Source for Medical Use. *Plasma Fus. Res.* **2019**, *14*, 3401160. [[CrossRef](#)]
29. Yoshida, M.; Hanada, M.; Kojima, A.; Kashiwagi, M.; Grisham, R.L.; Hatayama, A.; Shibata, T.; Yamamoto, T.; Akino, N.; Endo, Y.; et al. 22 A beam production of the uniform negative ions in the JT-60 negative ion source. *Fusion Eng. Des.* **2015**, *96–97*, 616–619. [[CrossRef](#)]
30. Takado, N.; Tobari, H.; Inoue, T.; Hanatani, J.; Hatayama, A.; Hanada, M.; Kashiwagi, M.; Sakamoto, K. Numerical analysis of the production profile of H^0 atoms and subsequent H^- ions in large negative ion sources. *J. Appl. Phys.* **2008**, *103*, 053302. [[CrossRef](#)]
31. Yoon, J.; Song, M.; Han, J.; Hwang, S.H.; Chang, W.; Lee, B.; Itikawa, Y. Cross sections for electron collisions with hydrogen molecules. *J. Phys. Chem. Ref. Data* **2008**, *37*, 913–931. [[CrossRef](#)]

Disclaimer/Publisher's Note: The statements, opinions and data contained in all publications are solely those of the individual author(s) and contributor(s) and not of MDPI and/or the editor(s). MDPI and/or the editor(s) disclaim responsibility for any injury to people or property resulting from any ideas, methods, instructions or products referred to in the content.